coatings

MDPI

Article

An Assessment of the Bactericidal and Virucidal Properties of ZrN-Cu Nanostructured Coatings Deposited by an Industrial PVD System

Sahand Behrangi [1,*], Ivo Sedláček [2], Ján Štěrba [3], Gabriela Suková [2], Zsolt Czigány [4], Vilma Buršíková [1], Pavel Souček [1], Vjačeslav Sochora [5], Katalin Balázsi [4] and Petr Vašina [1]

[1] Department of Physical Electronics, Faculty of Science, Masaryk University, Kotlářská 2, 61137 Brno, Czech Republic
[2] Department of Experimental Biology, Czech Collection of Microorganisms, Faculty of Science, Masaryk University, Kamenice 5, 625 00 Brno, Czech Republic
[3] Faculty of Science, University of South Bohemia, Branišovská 1760, 370 05 České Budějovice, Czech Republic
[4] Centre for Energy Research, Institute of Technical Physics and Materials Science, Konkoly Thege M. út 29-33, H-1121 Budapest, Hungary
[5] SHM, S.r.o., Průmyslová 3020/3, Šumperk 78701, Czech Republic
* Correspondence: behrangi@mail.muni.cz

Citation: Behrangi, S.; Sedláček, I.; Štěrba, J.; Suková, G.; Czigány, Z.; Buršíková, V.; Souček, P.; Sochora, V.; Balázsi, K.; Vašina, P. An Assessment of the Bactericidal and Virucidal Properties of ZrN-Cu Nanostructured Coatings Deposited by an Industrial PVD System. *Coatings* **2022**, *12*, 1330. https://doi.org/10.3390/coatings12091330

Academic Editors: Alistair Brydone, Dimitrios A. Lamprou, William McLean, Andrew I. M. Greer

Received: 19 August 2022
Accepted: 8 September 2022
Published: 12 September 2022

Publisher's Note: MDPI stays neutral with regard to jurisdictional claims in published maps and institutional affiliations.

Copyright: © 2022 by the authors. Licensee MDPI, Basel, Switzerland. This article is an open access article distributed under the terms and conditions of the Creative Commons Attribution (CC BY) license (https://creativecommons.org/licenses/by/4.0/).

Abstract: Pathogenic microbes, such as bacteria and viruses, can spread quickly via contaminated surfaces. Most of these pathogenic microorganisms can survive on surfaces for a long time. Touching these surfaces can lead to the transmission of the microorganisms to the human body and cause serious illnesses. ZrN-Cu coatings containing different amounts of Cu were deposited using an industrial PVD system, and their ability to inhibit bacteria and inactivate the SARS-CoV-2 virus was tested. Microstructural studies showed the formation of two distinct ZrN and Cu phases when Cu content was sufficiently high. Hardness and elastic modulus were inversely proportional to the Cu content. The coatings showed outstanding bactericidal properties against *Escherichia coli* and *Pseudomonas aeruginosa*, especially when Cu content was more than 12 at.% and exposure time was longer than 40 min. The coatings, however, did not exhibit any significant virucidal properties. Good mechanical properties, along with excellent antibacterial effects, make these coatings suitable for use as self-sanitizing surfaces on objects that people regularly touch and that are prone to bacterial contamination. Their use would thus allow for only minimal transmission or multiplication of bacteria, and the treated surface would not serve as another source of infection.

Keywords: magnetron sputtering; microstructure; crystallite size; bactericidal properties; SARS-CoV-2

1. Introduction

It is well-established that infectious microbes, such as bacteria, viruses, and microscopic fungi, can spread quickly via contaminated surfaces. Contamination is a risk for any frequently-touched surface, such as any kind of medical equipment in hospitals, door handles, fabrics, and so forth [1–6]. The development of antimicrobial coatings as a solution to this problem has attracted global interest, particularly in recent decades. Furthermore, there have been significant efforts to study and improve other properties of coatings, such as mechanical properties along with their antimicrobial efficiency, in order to make them multipurpose [7,8].

Antimicrobial or so-called self-sanitizing coatings can be categorized as passive or active. Passive coatings do not release any antimicrobial agents, and simply kill or inactivate pathogens upon contact. Conversely, active coatings release antimicrobial agents, such as antibiotics, antiseptics, and silver. Passive coatings are highly preferred over active because

they sustain their antimicrobial ability for extended periods, while most active coatings can release microbicides at effective concentrations only for several days [9,10].

Bacteria and viruses are the most common pathogenic microorganisms. Bacterial infection is a major clinical complication that can cause serious problems, especially considering the rising threat of antibiotic resistance. Most bacteria can survive on surfaces for long periods, depending on surface characteristics, the ambient, and the bacterium itself. Touching such surfaces, particularly in public places, is likely to transfer the adherent bacteria to the human body and consequently cause severe and even fatal illness. Hence, there has been an increasing interest in developing antibacterial coatings as a practical solution [11–14].

The recent outbreak of the COVID-19 disease has showed the necessity of developing antiviral surfaces to prevent the spread of pathogens through infected surfaces, especially in public places [15,16]. The pandemic has already claimed millions of lives worldwide and, more than ever, proved that viral infections are a serious global health challenge. Therefore, this area of study has attracted increased interest in the past two years [17–22].

Two well-known elements with outstanding bactericidal activity are silver (Ag) and copper (Cu). Both metals can inhibit bacteria upon contact. Thus, the fabrication and characterization of coatings containing either Cu [12,14,23,24] or Ag [25–29] has been extensively studied in recent years. Cu is preferable to Ag as it is an essential trace element and is metabolizable by the human body [30]. In contrast, silver tends to remain in the human body and increases the silver serum level [31]. Cu is a low-cost material with more remarkable bactericidal abilities due to the easier release of Cu^{2+} ions [32]. Moreover, Cu exhibits lower toxicity and higher cytocompatibility than Ag [33].

Zirconium nitride (ZrN) is a hard and wear-resistant material with a slight bactericidal effect [34–36]. Therefore, by incorporating a third element, such as Cu one can obtain specific properties, e.g., simultaneously good mechanical and bactericidal properties [30].

In this study, an industrial physical vapor deposition (PVD) system combining magnetron sputtering and arc evaporation methods was used to deposit ZrN-Cu coatings. The coatings were fabricated with varying copper contents to investigate the effect of copper concentration on the final properties. The efficiency of the coatings was assessed against two Gram-negative bacteria and the SARS-CoV-2 virus. It is worth mentioning that the principal novelty of this research, besides industrial production, is the use of a shorter bacterial exposure time compared to most of the testing procedures commonly found in the literature [11,14,30,37]. Short exposure times (typically only tens of minutes) were deliberately chosen to simulate a situation where exposed surfaces are touched frequently. This ensures an adequate self-sanitizing effect suitable for public places and frequently touched surfaces. ZrN-Cu can be an ideal coating for surfaces where both a self-sanitizing effect and good mechanical properties are expected. Door handles, for instance, are an excellent example of such a surface as they are susceptible to wear and to the transmission of pathogenic microorganisms. Therefore, ZrN as a hard protective coating combined with Cu as the bactericidal agent can be applied to door handles to enhance their longevity. In such applications, one must compromise between the mechanical and antimicrobial properties. The high production rate of industrial PVD systems is another factor that makes these coatings ideal for such applications.

2. Materials and Methods

2.1. Synthesis of the Coatings

All coatings were deposited using an industrial deposition system at SHM s.r.o. Šumperk, Czech Republic. The internal dimensions of the deposition chamber were 550 mm × 550 mm × 850 mm. A hybrid deposition procedure was utilized to combine arc evaporation (for Zr target) and magnetron sputtering (for Cu target) in a reactive atmosphere. The Zr target was made of Zr 702 alloy (99.2 wt.% Zr + Hf with Hf ≤ 4.5 wt.%, 0.8 wt.% Fe, Cr, O, C). The Cu target (99.95 wt.%) had a cylindrical shape with a diameter of 96 mm and length of 445 mm. The magnetron power was varied between 0.5 kW, 1 kW,

1.3 kW, 2.2 kW, and 3 kW in order to attain different copper contents. The other deposition parameters were kept constant: N_2 pressure 1.5 Pa, bias voltage −50 V, arc current 150 A, substrate temperature 400 °C, and total deposition time 60 min.

The coatings were deposited on Si (100) wafers with dimensions 15 mm × 15 mm. The substrates were ultrasonically pre-cleaned in an acetone and isopropanol bath. Before the deposition, the substrates underwent metal (Ti) ion etching for 9 min at an Ar flow rate of 35 sccm with a substrate bias voltage of −1000 V and a temperature of 400 °C. Afterward, an adhesion layer (ZrN) was deposited on the samples for 10 min, followed by the main ZrN-Cu coating process. After the deposition, the samples cooled down to the ambient temperature inside the chamber.

2.2. Analyses and Characterizations

A Tescan Mira3 Scanning Electron Microscope (SEM, Tescan, Brno, Czech Republic) equipped with Oxford Instruments X-Max^{50} X-ray Energy Dispersive Spectroscope (EDS, Oxford Instruments, Abingdon-on-Thames, UK) was employed to observe the microstructure and measure elemental composition. Quantification of the elemental composition was made using the internal standards library supplied by Oxford Instruments within the AZtec Software (Version 4.2, Oxford Instruments, Abingdon-on-Thames, UK). A Rigaku SmartLab Type F X-ray Diffractometer (XRD, Rigaku Corporation, Tokyo, Japan) in a Bragg-Brentano configuration with Cu Kα radiation (λ = 1.5418 Å) was employed to study the crystalline phase structure of the coatings. The size of the crystallites was determined from the XRD diffractograms using the Scherrer formula. The lattice parameter (a_0) was determined from the XRD diffractograms based on a_0 being directly proportional to interplanar spacing of the atomic planes (d) calculated from Bragg's law. Texture coefficients were calculated by dividing the intensity of the diffraction peaks by the intensity of the reference peak in the same diffractogram. Selected Area Electron Diffraction (SAED) patterns and EDS maps were obtained utilizing a C_s corrected 200 kV Themis (Thermo Fischer Scientific, Waltham, MA, USA) Transmission Electron Microscope (TEM). FIB lamellae for TEM investigations were prepared with Thermo Scientific Scios 2 Dual Beam equipment. The final steps in FIB preparation were made at 2 kV. A Hysitron TI950 Triboindenter (Bruker, Billerica, MA, USA) equipped with a Berkovich tip was used to measure hardness and elastic modulus. Photographs of the samples were taken under constant light conditions to determine the coloration of the coatings and afterwards color indices were determined from the raw files using the Zoner Photo Studio X software. The photos were taken with a Nikon D500 camera (Nikon Corporation, Tokyo, Japan) equipped with a Sigma DC 17–70 mm 1:2.8–4.5 lens.

2.3. Assessment of Bactericidal Properties

The bactericidal efficiency of the coatings was assessed by the plate-counting method. For this purpose, common bacteria usually present in human living environments were selected as follows: *Escherichia coli* (CCM 3988) and *Pseudomonas aeruginosa* (CCM 3955). The bacteria were obtained from the Czech Collection of Microorganisms (CCM), Masaryk University, Brno, Czech Republic. From the original 24 h culture on tryptone soya agar (TSA) at 37 °C, a 1° McFarland suspension in saline solution was prepared. Afterwards, the inoculum was twice diluted 1:10 down to the final inoculum (1:10 into the primary inoculum and then 1:10 again into the final inoculum) to reach 3×10^6 CFU/mL concentration. These concentrations were chosen after optimization to make final colony counting possible. 10 µL of the final inoculum was then pipetted onto the sterilized samples, covered with a coverslip, and incubated at room temperature and humidity for 20, 40, and 80 min. After incubation, the samples were put into 5 mL of saline solution and shaken at 37 °C for 10 min. Following the shaking, 100 µL of the suspension was pipetted onto TSA plates in triplicates, spread with a spreader, and incubated at 37 °C for 24 h. After 24 h the plates were taken out and colonies were enumerated.

The bactericidal efficiency (E) was calculated using the following Equation (1);

$$E(\%) = \frac{N_c - N_s}{N_c} \times 100 \quad (1)$$

where N_c is the number of bacteria colony-forming units (CFU) grown from the suspension that was in contact with the surface of the control sample (bare Si without any coating), and N_s is the number of bacterial colonies grown from the suspension that was in contact with the coated samples.

2.4. Assessment of Virucidal Properties

2.4.1. Virus and Cell Line

Vero E6 cells (African green monkey kidney cells, ATCC® CRL-1586) were grown in a DMEM low glucose medium supplemented with 10% fetal bovine serum, 1% L-glutamine, 100 U/mL penicillin, 100 μg/mL streptomycin, and 0.25 μg/mL amphotericin B at 37 °C and 5% CO_2. This cell line was used to passage the 118-181 SARS-CoV-2 isolate from the South Bohemian Region (lineage B.1.258, GISAID database acc. No. EPI_ISL_1702301, GenBank acc. No. OK180974). A cell medium containing the released virions was collected after infection for specific days and the viral titer was determined by plaque assay.

2.4.2. Plaque Assay

The number of infectious virus particles in the supernatant was determined by plaque assay [38]. 300 μL of Vero E6 cell suspension was added per well to a 24-well plate at the concentration of 5×10^5 cells/mL and left to adhere for 4 h at 37 °C with 0.5% CO_2. Then, 180 μL of a decimally diluted viral sample in a complete DMEM medium was added to each well and left for 2 h to incubate. Cells were overlayed with 400 μL of 1.5% carboxymethylcellulose in a complete DMEM medium and incubated for 3 days at 37 °C with 0.5% CO_2. Afterward, the cells were washed with 0.9% NaCl and fixed and stained for 40 min with 0.1% Naphthalene black (Sigma-Aldrich, Hamburg, Germany) in 6% acetic acid (Lach-Ner, Neratovice, Czech Republic). Plaque counts were determined as PFU/mL and compared to the positive control.

2.4.3. qRT-PCR Quantitation of SARS-CoV-2 Viral RNA

RNA was extracted from 200 μL of the cell medium containing SARS-CoV-2 virions using the Nucleic Acid Extraction Kit B-200 and the EXM3000 Nucleic Acid Isolation System (Zybio, Chongqing, China). qRT-PCR was performed using the Allplex 2019-nCoV Assay kit (Seegene, Seoul, South Korea) in the CFX96 Touch Real-Time PCR cycler System (Bio-Rad, Hercules, CA, USA). Relative quantification of RNA copies was calculated using the ΔΔCt method.

3. Results and Discussions

3.1. Mechanical Properties and Chemical Composition

The coatings were deposited with varying copper amounts to study the impact of Cu concentration on the resultant properties. This was done by varying the power of the Cu target in the range of 0.5–3 kW. The deposited samples were labeled based on their Cu content. Table 1 shows the notations of the samples as well as the applied power, chemical composition, deposition rate and mechanical properties. The thickness of the coatings measured by SEM was 1–1.35 μm.

Table 1 also shows that the Cu content of the coatings was directly proportional to the power applied to the Cu target. Moreover, as the Cu content increased, the amount of Zr and N decreased jointly at the same rate, suggesting that N was consumed exclusively by Zr. It is worth mentioning that all samples contained 2–7 at.% of C and 2–3 at.% of O and these correspond to contamination from the atmosphere together with 0.3–0.5 at.% of

Hf that comes from the Zr target. As all these percentages are low, these are taken as contaminants and are not taken into consideration further. EDS spectra of the coatings are shown in Figure S1.

Table 1. Chemical composition, deposition rate, and the mechanical properties of the ZrN-Cu coatings with different Cu content.

Sample	Cu Target Power (kW)	Cu (at.%)	Zr (at.%)	N (at.%)	Deposition Rate (nm/min)	Hardness (GPa)	Elastic Modulus (GPa)
Cu0	0.5	0.6	50.7	48.7	19	28.5 ± 0.8	336 ± 9
Cu6	1	6.7	47.1	46.2	19	28.0 ± 0.5	304 ± 4
Cu12	1.3	12.8	43.2	44.0	21	24.2 ± 0.7	299 ± 8
Cu25	2.2	25.8	36.9	37.3	17	17.8 ± 0.3	242 ± 7
Cu29	3	29.8	34.9	35.3	22	15.1 ± 0.4	242 ± 5

The mechanical properties of the ZrN-Cu coatings showed a clear relation between microhardness and Cu content. This is demonstrated by Figure 1. They show that incorporating ~30 at.% Cu to ZrN resulted in a hardness decrease from 28.5 ± 0.8 GPa to 15.1 ± 0.4 GPa. The same trend is seen for the elastic modulus, which exhibited a fall from 336 ± 9 GPa to 242 ± 5 GPa. This will be discussed further in the microstructure section. Other authors have reported a similar trend for mechanical properties when increasing the additive element to ZrN or TiN [39–41]. However, Musil et al. [30] observed an initial enhancement in mechanical properties when the Cu content was low (<2 at.%), followed by a gradual decrease. The same was reported by Zeman et al. [42], where samples with 1–2 at.% Cu exhibited higher hardness.

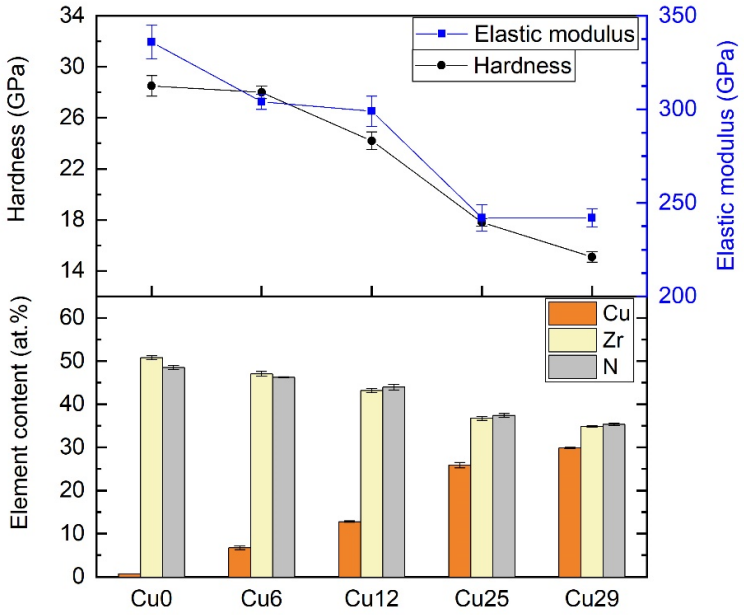

Figure 1. Chemical composition and mechanical properties of ZrN-Cu coatings.

3.2. The Coloration of the Coatings

For some applications the appearance of the coating can be of particular importance. Therefore, the coloration of the coatings was measured for comparison. Figure 2 represents the coloration indices of the coatings in the CIELAB or *L*a*b** color space. In this space, there are three coordinates; (1) *L** represents the lightness of the color, (2) *a** shows

the position of the color between red and green (negative values indicate green and positive values indicate red), and (3) *b** shows the position of the color between yellow and blue (negative values indicate blue and positive values indicate yellow).

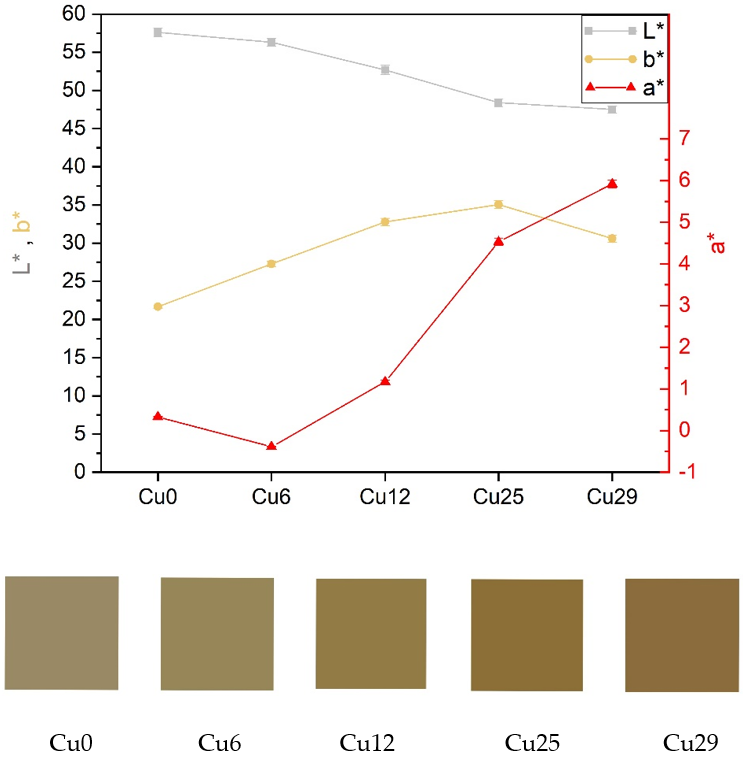

Figure 2. Coloration of the ZrN-Cu coatings in *L*a*b** space.

The color of the coatings gradually became reddish following increases in Cu content. Figure 2 shows that *L** reached its lowest value when the Cu content was highest (Cu29), implying that increasing the copper content led to the darkening of the coating. Furthermore, more Cu content increased the *a** value, indicating a more reddish color. *b** (the level of yellow color) increased with Cu content and reached its peak at Cu25, followed by a drop when the Cu content increased beyond 25 at.%.

3.3. Microstructure

The XRD patterns of the coatings are shown in Figure 3. The vertical dashed lines indicate the reference positions of ZrN and Cu phases according to the PDF cards 00-035-0753 and 00-004-0836, respectively. The pattern obtained for the Cu0 sample exhibited only ZrN reflections with dominant (200) and (311) reflections. However, Cu incorporation led to a change in the preferential growth orientation of ZrN. This change occurred at the expense of mostly eliminating the (311) reflection. ZrN peaks shifted to higher diffraction angles with Cu incorporation. The peak shift implies a distortion of the lattice induced by the dissolution of Cu in ZrN. The ZrN lattice likely contracted due to the substitution of Zr by Cu atoms as Cu has a smaller atomic radius than Zr [43]. Lattice contraction means smaller interplanar spacing and, consequently, higher diffraction angles. It is evident that the degree of peak shift should correlate with the amount of incorporated Cu, i.e., greater Cu amounts lead to higher 2θ positions of ZrN peaks.

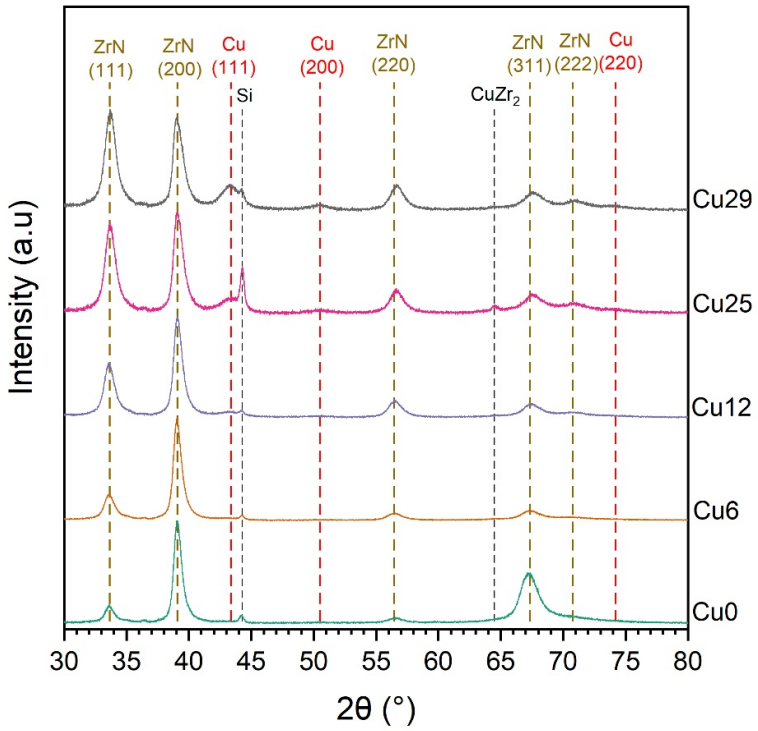

Figure 3. XRD patterns of ZrN-Cu coatings with different copper contents. Si diffractions originate from the substrate.

Cu6 did not show any Cu reflection, which implies that most Cu atoms were either substitutionally incorporated within ZrN grains or located randomly at the sites of defects, such as grain boundaries as suggested by [39]. If any Cu grains formed in Cu6, they were very fine and could not be detected by XRD. Cu12 already exhibited a very weak Cu peak, corresponding to the (111) reflection (Figure 3). Similar results have been reported by other authors confirming that when the Cu content was low, no Cu crystalline phase was observed. Musil et al. [30] and Chen et al. [44] detected Cu crystalline phase when Cu content was more than 9 at.% and 6 at.%, respectively. The diffractograms from the Cu25 and Cu29 samples showed distinct Cu(111) peaks of higher intensity and the emergence of a weak Cu(200) reflection. This indicates that increasing the Cu content of the coating led to the formation of a separate Cu phase. Hence, Cu atoms lay not only in the ZrN lattice but also in the grain boundaries and formed a distinct second phase. The copper incorporation in ZrN lattice will reach a saturation limit at a certain copper content. Determination of such a limit requires further experiments on the samples with higher copper contents, which was beyond the scope of this work. The existence of metallic Cu, even in a pure nitrogen atmosphere, can be explained by the fact that Cu_3N is thermally unstable and decomposes into copper and nitrogen. In the literature various thermal decomposition temperatures (mostly up to 450 °C) have been reported for Cu_3N [45–53]. Since copper nitride decomposes into pure Cu at low temperatures, reactive co-deposition of Cu and Zr in the presence of nitrogen at elevated temperatures resulted in the formation of ZrN and Cu phases [30,32,42,53,54].

Figure 4 shows the evolution of the lattice parameter and the crystallite size based on copper content. The lattice parameter decreases due to the substitution of Zr with Cu and the contraction of the ZrN lattice. Figure 4 indicates a slight decrease in the size of ZrN crystallites with increasing Cu content. The smallest ZrN crystallite is obtained for Cu29. This trend can be attributed to the formation of a distinct Cu phase. As seen in Figure 3, increased Cu concentrations lead to a partial segregation of Cu to form an additional Cu phase, which might have blocked the growth of ZrN [42].

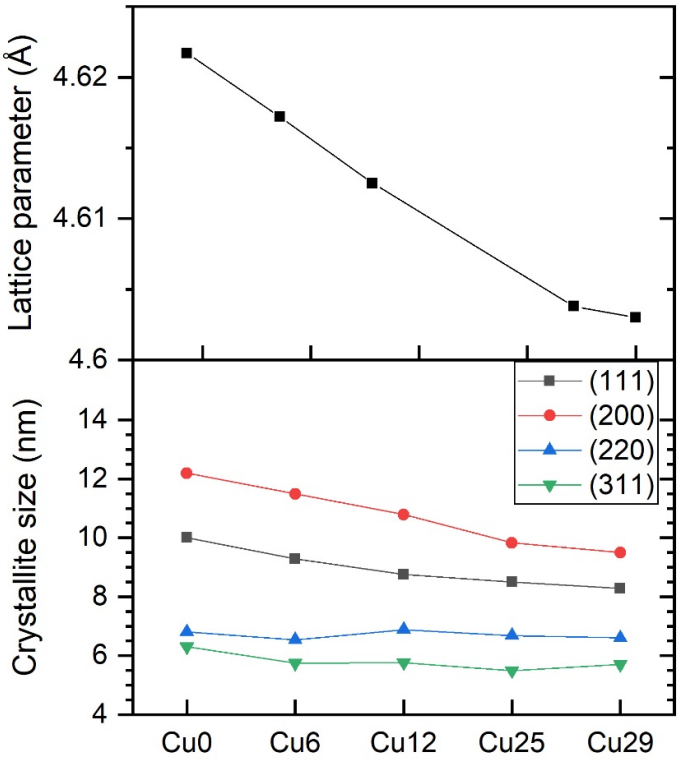

Figure 4. The lattice parameter, and crystallite size of ZrN-Cu coatings with different copper contents.

The coatings did not follow the Hall–Petch relation, where hardness increases inversely to the square root of the grain size. As the observed grain sizes were small, the reverse Hall-Petch effect was rather observed. This effect takes place when the grain size is less than approximately 13 nm [55]. When the grains are finer than ~13 nm, grain boundary sliding is assumed to be responsible for the reduction in strength. Softening caused by grain boundary sliding is attributed mainly to grain boundary defects, which allow for fast diffusion of atoms and vacancies under stress [56]. Furthermore, the possible existence of a Cu phase at the grain boundaries might be the other reason for worsening of the mechanical properties. This behavior can be attributed to the low hardness and elastic modulus of the copper phase, which can affect the mechanical properties of the whole coating according to the law of mixtures of composite material [13].

Figure 5 shows the texture coefficients for the different orientations. ZrN(111) was chosen as the reference peak because it has the highest relative intensity in the PDF card and the other texture coefficients were calculated in relation to (111). This figure indicates that Cu content significantly affected the texture coefficients of the coatings. As Cu increased in the coating, the texture coefficients fall abruptly to values close to the reference ZrN (dashed lines).

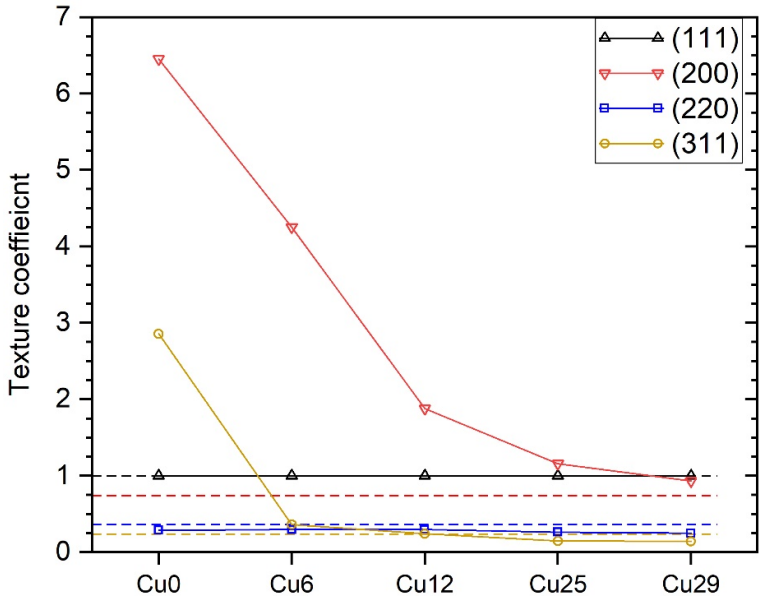

Figure 5. Texture coefficients of the ZrN-Cu coatings. The dashed lines indicate the relative intensity of ZrN diffractions in PDF card 00-035-0753.

To further analyze the microstructure, a TEM analysis was performed to obtain the Selected Area Electron Diffraction (SAED) patterns. Figure 6 presents the SAED patterns of Cu6, Cu12, Cu25, and Cu29 samples. The SAED pattern of Cu6 shows only ZrN reflections, and no Cu ring is observed. The emergence of a Cu(111) ring, albeit faintly, in the SAED pattern of Cu12 supports the idea of the formation of a separate crystalline Cu phase. In the case of Cu25, another diffraction ring corresponding to Cu(200) appears, and with a further increase in copper content to ~29 at.%, the Cu(200) ring becomes slightly stronger.

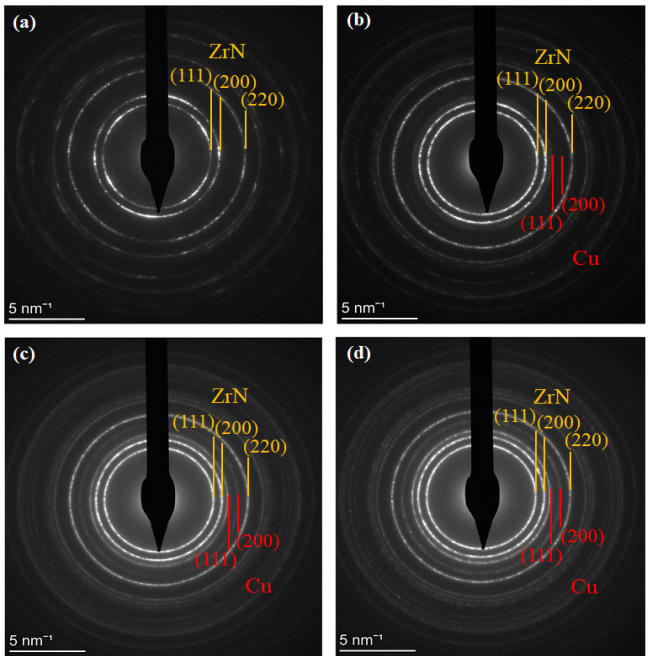

Figure 6. SAED patterns of (**a**) Cu6; (**b**) Cu12; (**c**) Cu25; and (**d**) Cu29.

The SAED patterns suggest polycrystallinity of the coatings, with grains almost randomly oriented. However, as seen in their SAED patterns, the ZrN rings of Cu6 and Cu12

were not entirely continuous. This implies the presence of a certain amount of texture in the coatings. Because the texture coefficients of Cu25 and Cu29 were lower, their diffraction rings became more continuous compared to Cu6 and Cu12. As discussed above, the SAED results agree with the XRD results presented in Figures 3 and 5.

A TEM-EDS map of the Cu29 sample (Figure 7) shows the dispersion of Zr, N, and Cu in the coating. In this map, the green color is assigned to Cu and red color is assigned to Zr. The images show almost no N in Cu accumulation sites, which is likely due to the lack of chemical bonds between them.

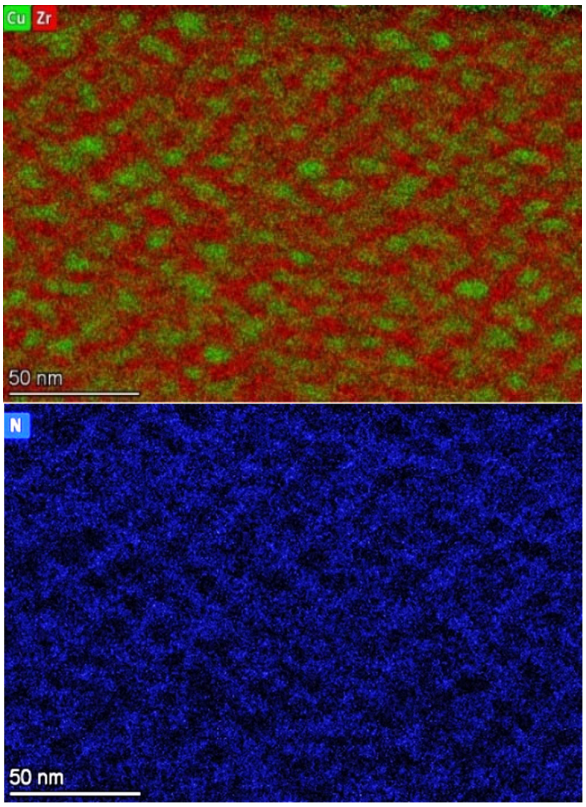

Figure 7. Cu/Zr (top) and N (bottom) TEM-EDS maps of the Cu29 sample.

3.4. Bactericidal Properties

To evaluate the bactericidal properties of coatings, various species of bacteria are usually used, such as *Escherichia coli* [11,30,57], *Staphylococcus aureus* [31,36], *Pseudomonas aeruginosa* [27], or *Staphylococcus epidermidis* [31,58]. This study evaluated the bactericidal activity of Cu-containing coatings against species with which humans are frequently in contact. For this purpose, two Gram-negative bacteria were chosen: (1) *Escherichia coli*, a gut bacterium, and a major foodborne pathogen. *E. coli* can cause diarrhea and bloodstream infections, which frequently lead to hospitalization [59], and (2) *Pseudomonas aeruginosa*, which is frequently associated with hospital-acquired infections due to its ability to survive under challenging environmental conditions. *P. aeruginosa* can be highly pathogenic in susceptible patients and can cause high morbidity and mortality among immunocompromised patients [59,60].

The bactericidal activity of the surface is characterized by its efficiency at killing bacteria (E) settled on the surface according to Equation (1). Figure 8 shows the bactericidal efficiency of ZrN-Cu coatings with different Cu concentrations against *E. coli* and *P. aeruginosa*. The contact time of the bacteria with the surface varied, either 20, 40, or 80 min. As evident in this figure, the bactericidal efficiency of the coatings strongly depended on the

Cu concentration. In shorter exposure times, a strange behavior was sometimes observed, as seen in Figure 8. A larger sample set would determine the actual course for each sample type. This trajectory was not critical as it happened only in low copper amount containing samples, which did not show sufficient bactericidal efficiency and are unsuitable for self-sanitizing applications. The values of bactericidal efficiency may differ depending on the species used for the test. These differences are often attributed to the thickness and composition of the bacteria's cell wall and the bactericidal agent's ability to penetrate it [61]. As seen in Figure 8, *E. coli* is more resistant than *P. aeruginosa*. For instance, the copper amount had to be at least 25 at.% to kill almost all *E. coli* colonies in 40 min. However, in the case of *P. aeruginosa*, 12 at.% Cu sufficed to obtain a bactericidal efficiency of ~100%. Other authors have reported similar results. For instance, Musil et al. [30] observed 100% bactericidal efficiency of ZrN-Cu coatings containing Cu > 10 at.% after 5 h exposure time.

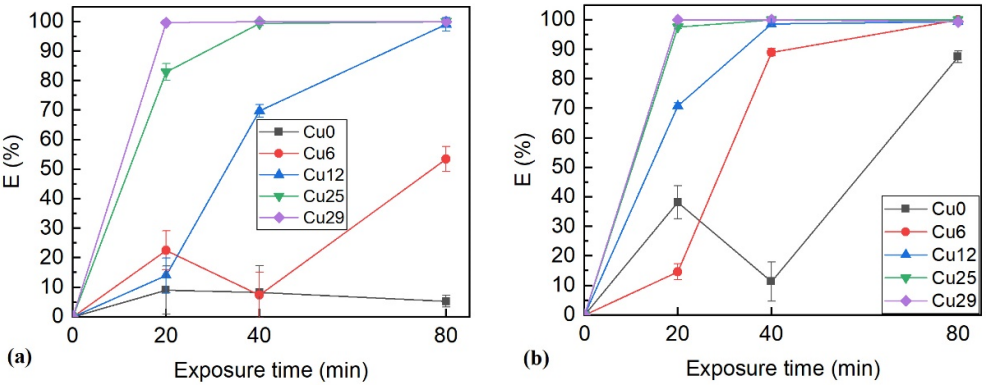

Figure 8. Bactericidal efficiency of ZrN-Cu coatings against (**a**) *E. coli*; (**b**) *P. aeruginosa* at different exposure times.

Even though substantial work has been performed to address the mechanism of eradicating bacteria upon contact with copper, some aspects of copper's antibacterial mechanism still need clarification. One key element that initiates the so-called "contact killing" is the release of Cu ions from the Cu-containing surface. The released ions are capable of damaging the cell membrane, followed by membrane degradation and penetration of copper-released ions into the cell. Eventually, the DNA of the bacterium is destroyed by the penetrant ions [23,24].

3.5. Virucidal Properties

The virucidal ability of the ZrN-Cu coatings was evaluated against SARS-CoV-2 and presented in Figure 9. For this purpose, viral suspension in a suitable buffer solution was added onto the studied ZrN-Cu coatings and incubated for specific intervals. It is worth mentioning that there is a difference between bacteria and viruses. Bacteria do not die by themselves and even with a low amount of nutrients they begin to replicate. On the contrary, virions in a solution decompose at a certain rate and lose their ability to infect cells. In other words, when a bacterial suspension is prepared at the beginning of an experiment, no lowering of bacterial counts (CFU) is expected. Therefore, one merely needs to observe how the CFU lowers throughout the experiment upon contact with a surface. Virion numbers, however, decrease over time. Hence, two control samples are needed: a sample in a medium as the positive control and an uncoated sample as the negative control. Si wafers were cut into the same dimensions as the test samples and were used as negative controls.

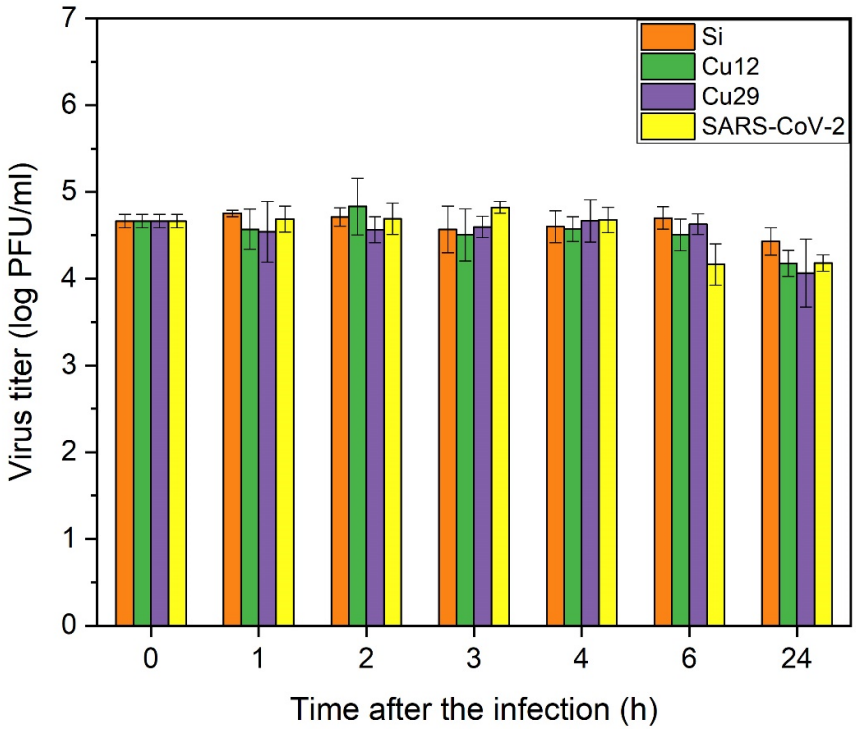

Figure 9. Antiviral effect of Cu12 and Cu29 coatings against SARS-CoV-2. Si was chosen as the negative control, which is shown by orange color.

As seen in Figure 9, a comparison of the positive control results (SARS-CoV-2) reveals a significant decrease in plaque-forming units (PFU) over time. This indicates that the virions became inactivated over time, even alone in the solution. Comparing PFU of the positive control with the test samples showed no significant difference in the virus titer. Thus, the ZrN-Cu coatings did not have a virucidal effect against SARS-CoV-2 and the viral titer decreased in time even without any active surfaces. The antiviral effect was evaluated in the first 24 h as most of the infectious particles are inactivated in the first hours on smooth surfaces [62], and an antiviral effect of a coating should primarily act in this time frame.

To observe a significant antiviral effect, one needs to ideally obtain a zero virus titer, or at least a reduction of more than one order of magnitude in the examined samples. The antiviral effect of copper is a well-known phenomenon that has been presented in numerous works [63–66]. The recent outbreak of COVID-19 has attracted the interest of researchers to study the ability of copper to inactivate the SARS-CoV-2 virus as well [66-68].

To assess the ability of pure copper to inactivate SARS-CoV-2, Cu coating was deposited by magnetron sputtering and its virucidal activity was tested. Figure 10 shows a significant virucidal activity of copper coating on a Si wafer substrate against the SARS-CoV-2 virus, which agrees with other published data, for example, in [69].

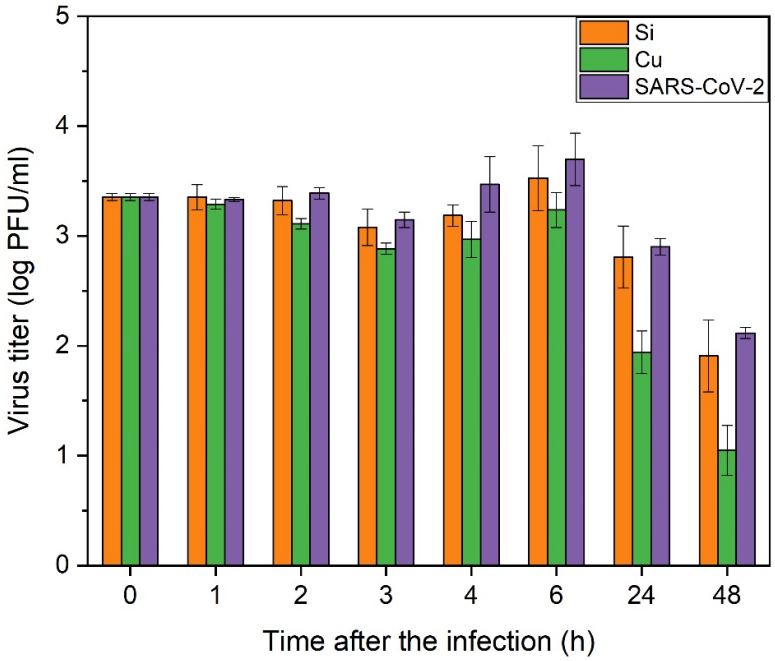

Figure 10. Antiviral effect of pure copper coating against SARS-CoV-2. Si was chosen as the negative control, which is shown by orange color.

The antiviral activity of surfaces with high copper content is mediated by various mechanisms, most probably membrane damage or viral genomic nucleic acid fragmentation. However, the exact mechanism of the copper antiviral effect has not been elucidated yet [70].

It seems that the Cu content in the studied ZrN-Cu samples was insufficient to inactivate a significant number of viral particles. Increasing the copper content of the coatings could not be an appropriate solution as the durability of the coating is also essential for real-life applications. The primary purpose of this study was to deposit antimicrobial coatings with good mechanical properties. However, incorporating ~30 at.% Cu already decreased hardness by ~47% and elastic modulus by ~28%, and further softening of the coating would not be acceptable from a mechanical properties point of view. Other possibilities to increase the antiviral activity of the studied coatings could be the introduction of materials producing reactive oxygen species, such as titanium oxide [71].

4. Conclusions

ZrN-Cu coatings containing different amounts of Cu were deposited using an industrial scale PVD system combining arc evaporation of Zr and magnetron sputtering of Cu in a nitrogen atmosphere. The hardness and elastic modulus both decrease with the Cu content of the coating. It was observed that when the copper content is ~6 at.%, the microstructure comprises only the crystalline ZrN phase, indicating Cu substitution of Zr in ZrN. However, increasing Cu content leads to the formation of crystalline Cu as the second phase in the microstructure. Copper concentration significantly influences bactericidal efficiency. Even following short exposure times of several tens of minutes, the coatings show outstanding bactericidal effects against *E. coli* and *P. aeruginosa*, however *E. coli* behaves more resistantly than *P. aeruginosa*. In conclusion, hard, wear-resistant ZrN-Cu coatings have the potential for development towards industrial applications and be applied to surfaces that people regularly touch to prevent the spread of bacterial infections. The copper concentration of such a coating should be between 13 and 25 at.%, depending on the application, to find an appropriate balance between the mechanical properties and the antibacterial efficiency. Such coatings could be suitable for highly exposed areas, such as hospitals, public spaces, and social institutions. It should be mentioned that, prior to

scaling up, further experiments should be done to evaluate the durability and efficiency of these coatings under real working conditions over time. For instance, wash-out elution analysis can be performed to determine whether the copper ions dissipate from the coating material over time. Furthermore, assessing the efficiency of such coatings against Gram-positive bacteria could be beneficial as they can behave differently upon contact with antibacterial surfaces. As for the antiviral properties, developing hybrid materials that produce reactive ion species can be a promising area of study.

Supplementary Materials: EDS spectra of the ZrN-Cu coatings are available online at: www.mdpi.com/article/10.3390/coatings12091330/s1.

Author Contributions: Conceptualization, S.B., P.V. and I.S.; methodology, S.B., I.S., G.S., V.S., Z.C., P.S. and J.Š.; validation, S.B.; investigation, S.B., P.S., Z.C., G.S., J.Š. and V.B.; writing—original draft preparation, S.B. and J.S; writing—review and editing, S.B., P.V., J.Š., I.S., Z.C. and P.S.; visualization, S.B.; supervision, P.V.; funding acquisition, P.V. and K.B. All authors have read and agreed to the published version of the manuscript.

Funding: This research has been supported by project LM2018097 funded by the Ministry of Education, Youth and Sports of the Czech Republic. This work was also supported by the grant no. VEKOP-2.3.3-15-2016-00002 and VEKOP-2.3.2-16-2016-00011 of the European Structural and Investment Funds.

Institutional Review Board Statement: Not applicable.

Informed Consent Statement: Not applicable.

Data Availability Statement: Not applicable.

Acknowledgments: The authors would like to acknowledge Péter B. Barna for his kind help with the microstructural studies and Katarína Bernátová for assisting with the coloration measurements.

Conflicts of Interest: The authors declare no conflict of interest.

References

1. Potter, B.A.; Lob, M.; Mercaldo, R.; Hetzler, A.; Kaistha, V.; Khan, H.; Kingston, N.; Knoll, M.; Maloy-Franklin, B.; Melvin, K.; et al. A long-term study examining the antibacterial effectiveness of Agion silver zeolite technology on door handles within a college campus. *Lett. Appl. Microbiol.* **2015**, *60*, 120–127. https://doi.org/10.1111/lam.12356.
2. El-Rafie, M.H.; Ahmed, H.B.; Zahran, M.K. Characterization of nanosilver coated cotton fabrics and evaluation of its antibacterial efficacy. *Carbohydr. Polym.* **2014**, *107*, 174–181. https://doi.org/10.1016/j.carbpol.2014.02.024.
3. Page, K.; Wilson, M.; Parkin, I.P. Antimicrobial surfaces and their potential in reducing the role of the inanimate environment in the incidence of hospital-acquired infections. *J. Mater. Chem.* **2009**, *19*, 3818–3831. https://doi.org/10.1039/b818698g.
4. Burke, G.H.; Butler, J.P. Analysis of the role of copper impregnated composite hard surfaces, bed linens and patient gowns in reducing healthcare-associated infection rates. *Int. J. Infect. Control* **2018**, *14*, 1–8. https://doi.org/10.3396/ijic.v14i1.005.18.
5. Wickens, D.J.; West, G.; Kelly, P.J.; Verran, J.; Lynch, S.; Whitehead, K.A. Antimicrobial activity of nanocomposite zirconium nitride/silver coatings to combat external bone fixation pin infections. *Int. J. Artif. Organs* **2012**, *35*, 817–825. https://doi.org/10.5301/ijao.5000156.
6. Simoncic, B.; Tomsic, B. Structures of Novel Antimicrobial Agents for Textiles—A Review. *Text. Res. J.* **2010**, *80*, 1721–1737. https://doi.org/10.1177/0040517510363193.
7. Chen, N.H.; Chung, C.J.; Chiang, C.C.; Chen, K.C.; He, J.L. Antimicrobial copper-containing titanium nitride coatings Co-deposited by arc ion plating/magnetron sputtering for protective and decorative purposes. *Surf. Coat. Technol.* **2014**, *253*, 83–88. https://doi.org/10.1016/j.surfcoat.2014.05.017.
8. Kelly, P.J.; Li, H.; Benson, P.S.; Whitehead, K.A.; Verran, J.; Arnell, R.D.; Iordanova, I. Comparison of the tribological and antimicrobial properties of CrN/Ag, ZrN/Ag, TiN/Ag, and TiN/Cu nanocomposite coatings. *Surf. Coat. Technol.* **2010**, *205*, 1606–1610. https://doi.org/10.1016/j.surfcoat.2010.07.029.
9. Zhao, L.; Chu, P.K.; Zhang, Y.; Wu, Z. Antibacterial coatings on titanium implants. *J. Biomed. Mater. Res. Part B Appl. Biomater.* **2009**, *91*, 470–480. https://doi.org/10.1002/jbm.b.31463.
10. Qin, S.; Xu, K.; Nie, B.; Ji, F.; Zhang, H. Approaches based on passive and active antibacterial coating on titanium to achieve antibacterial activity. *J. Biomed. Mater. Res. Part A* **2018**, *106*, 2531–2539. https://doi.org/10.1002/jbm.a.36413.
11. Tian, X.B.; Wang, Z.M.; Yang, S.Q.; Luo, Z.J.; Fu, R.K.Y.; Chu, P.K. Antibacterial copper-containing titanium nitride films produced by dual magnetron sputtering. *Surf. Coat. Technol.* **2007**, *201*, 8606–8609. https://doi.org/10.1016/j.surfcoat.2006.09.322.
12. Wang, J.; Zhao, B.; Li, G.; Yang, K.; Yu, J.; Yang, X.; Zhan, D. Study of TiCu/TiCuN multilayer films with antibacterial activity. *Mater. Technol.* **2020**, *35*, 475–482. https://doi.org/10.1080/10667857.2019.1699269.

13. Mejía, H.D.; Echavarría, A.M.; Bejarano, G., G. Influence of Ag-Cu nanoparticles on the microstructural and bactericidal properties of TiAlN(Ag,Cu) coatings for medical applications deposited by Direct Current (DC) magnetron sputtering. *Thin Solid Film.* **2019**, *687*, 137460. https://doi.org/10.1016/j.tsf.2019.137460.
14. Sharifahmadian, O.; Salimijazi, H.R.; Fathi, M.H.; Mostaghimi, J.; Pershin, L. Relationship between surface properties and antibacterial behavior of wire arc spray copper coatings. *Surf. Coat. Technol.* **2013**, *233*, 74–79. https://doi.org/10.1016/j.surfcoat.2013.01.060.
15. Birkett, M.; Dover, L.; Lukose, C.C.; Zia, A.W.; Tambuwala, M.M.; Serrano-Aroca, Á. Recent Advances in Metal-Based Antimicrobial Coatings for High-Touch Surfaces. *Int. J. Mol. Sci.* **2022**, *23*, 1162. https://doi.org/10.3390/ijms23031162.
16. Wang, N.; Ferhan, A.R.; Yoon, B.K.; Jackman, J.A.; Cho, N.J.; Majima, T. Chemical design principles of next-generation antiviral surface coatings. *Chem. Soc. Rev.* **2021**, *50*, 9741–9765. https://doi.org/10.1039/d1cs00317h.
17. Balagna, C.; Francese, R.; Perero, S.; Lembo, D.; Ferraris, M. Nanostructured composite coating endowed with antiviral activity against human respiratory viruses deposited on fibre-based air filters. *Surf. Coat. Technol.* **2021**, *409*, 126873. https://doi.org/10.1016/j.surfcoat.2021.126873.
18. Mittireddi, R.T.; Patel, N.M.; Gautam, A.R.S.; Soppina, V.; Panda, E. Non-stoichiometric amorphous TiOx as a highly reactive, transparent anti-viral surface coating. *J. Alloys Compd.* **2021**, *881*, 160610. https://doi.org/10.1016/j.jallcom.2021.160610.
19. Meister, T.L.; Fortmann, J.; Breisch, M.; Sengstock, C.; Steinmann, E.; Köller, M.; Pfaender, S.; Ludwig, A. Copper and silver thin film systems display differences in antiviral and antibacterial properties-implications for the prevention of SARS-CoV-2 infections. *arXiv* **2021**, arXiv:2106.11606.
20. Butot, S.; Baert, L.; Zubera, A.S. Assessment of Antiviral Coatings for High-Touch Surfaces by Using Human Coronaviruses Hcov-229e and Sars-Cov-2. *Appl. Environ. Microbiol.* **2021**, *87*, 1–8. https://doi.org/10.1128/AEM.01098-21.
21. Rakowska, P.D.; Tiddia, M.; Faruqui, N.; Bankier, C.; Pei, Y.; Pollard, A.J.; Zhang, J.; Gilmore, I.S. Antiviral surfaces and coatings and their mechanisms of action. *Commun. Mater.* **2021**, *2*, 53. https://doi.org/10.1038/s43246-021-00153-y.
22. Basak, S.; Packirisamy, G. Nano-based antiviral coatings to combat viral infections. *Nano-Struct. Nano-Objects* **2020**, *24*, 100620. https://doi.org/10.1016/j.nanoso.2020.100620.
23. Luo, J.; Hein, C.; Mücklich, F.; Solioz, M. Killing of bacteria by copper, cadmium, and silver surfaces reveals relevant physicochemical parameters. *Biointerphases* **2017**, *12*, 020301. https://doi.org/10.1116/1.4980127.
24. Vincent, M.; Duval, R.E.; Hartemann, P.; Engels-Deutsch, M. Contact killing and antimicrobial properties of copper. *J. Appl. Microbiol.* **2018**, *124*, 1032–1046. https://doi.org/10.1111/jam.13681.
25. Shimazaki, T.; Miyamoto, H.; Ando, Y.; Noda, I.; Yonekura, Y.; Kawano, S.; Miyazaki, M.; Mawatari, M.; Hotokebuchi, T. In vivo antibacterial and silver-releasing properties of novel thermal sprayed silver-containing hydroxyapatite coating. *J. Biomed. Mater. Res. Part B Appl. Biomater.* **2010**, *92*, 386–389. https://doi.org/10.1002/jbm.b.31526.
26. Ju, H.; Yu, D.; Yu, L.; Ding, N.; Xu, J.; Zhang, X.; Zheng, Y.; Yang, L.; He, X. The influence of Ag contents on the microstructure, mechanical and tribological properties of ZrN-Ag films. *Vacuum* **2018**, *148*, 54–61. https://doi.org/10.1016/j.vacuum.2017.10.029.
27. Fielding, G.A.; Roy, M.; Bandyopadhyay, A.; Bose, S. Antibacterial and biological characteristics of silver containing and strontium doped plasma sprayed hydroxyapatite coatings. *Acta Biomater.* **2012**, *8*, 3144–3152. https://doi.org/10.1016/j.actbio.2012.04.004.
28. Chen, W.; Liu, Y.; Courtney, H.S.; Bettenga, M.; Agrawal, C.M.; Bumgardner, J.D.; Ong, J.L. In vitro anti-bacterial and biological properties of magnetron co-sputtered silver-containing hydroxyapatite coating. *Biomaterials* **2006**, *27*, 5512–5517. https://doi.org/10.1016/j.biomaterials.2006.07.003.
29. Kelly, P.J.; Li, H.; Whitehead, K.A.; Verran, J.; Arnell, R.D.; Iordanova, I. A study of the antimicrobial and tribological properties of TiN/Ag nanocomposite coatings. *Surf. Coat. Technol.* **2009**, *204*, 1137–1140. https://doi.org/10.1016/j.surfcoat.2009.05.012.
30. Musil, J.; Zítek, M.; Fajfrlík, K.; Čerstvý, R. Flexible antibacterial Zr-Cu-N thin films resistant to cracking. *J. Vac. Sci. Technol. A.* **2016**, *34*, 021508. https://doi.org/10.1116/1.4937727.
31. Stranak, V.; Wulff, H.; Rebl, H.; Zietz, C.; Arndt, K.; Bogdanowicz, R.; Nebe, B.; Bader, R.; Podbielski, A.; Hubicka, Z.; et al. Deposition of thin titanium-copper films with antimicrobial effect by advanced magnetron sputtering methods. *Mater. Sci. Eng. C* **2011**, *31*, 1512–1519. https://doi.org/10.1016/j.msec.2011.06.009.
32. Kumar, D.D.; Kaliaraj, G.S. Multifunctional zirconium nitride/copper multilayer coatings on medical grade 316L SS and titanium substrates for biomedical applications. *J. Mech. Behav. Biomed. Mater.* **2018**, *77*, 106–115. https://doi.org/10.1016/j.jmbbm.2017.09.007.
33. Hadrup, N.; Sharma, A.K.; Loeschner, K. Toxicity of silver ions, metallic silver, and silver nanoparticle materials after in vivo dermal and mucosal surface exposure: A review. *Regul. Toxicol. Pharmacol.* **2018**, *98*, 257–267. doi: 10.1016/j.yrtph.2018.08.007.
34. Ji, M.K.; Park, S.W.; Lee, K.; Kang, I.C.; Yun, K.D.; Kim, H.S.; Lim, H.P. Evaluation of antibacterial activity and osteoblast-like cell viability of TiN, ZrN and (Ti1-xZrx)N coating on titanium. *J. Adv. Prosthodont.* **2015**, *7*, 166–171. https://doi.org/10.4047/jap.2015.7.2.166.
35. Brunello, G.; Brun, P.; Gardin, C.; Ferroni, L.; Bressan, E.; Meneghello, R.; Zavan, B.; Sivolella, S. Biocompatibility and antibacterial properties of zirconium nitride coating on titanium abutments: An in vitro study. *PLoS ONE* **2018**, *13*, e0199591. https://doi.org/10.1371/journal.pone.0199591.
36. Ramoul, C.; Beliardouh, N.E.; Bahi, R.; Nouveau, C.; Djahoudi, A.; Walock, M.J. Surface performances of PVD ZrN coatings in biological environments. *Tribol. Mater. Surf. Interfaces* **2019**, *13*, 12–19. https://doi.org/10.1080/17515831.2018.1553820.

37. Peng, C.; Zhao, Y.; Jin, S.; Wang, J.; Liu, R.; Liu, H.; Shi, W.; Kolawole, S.K.; Ren, L.; Yu, B.; et al. Antibacterial TiCu/TiCuN Multilayer Films with Good Corrosion Resistance Deposited by Axial Magnetic Field-Enhanced Arc Ion Plating. *ACS Appl. Mater. Interfaces* **2019**, *11*, 125–136. https://doi.org/10.1021/acsami.8b14038.
38. Baer, A.; Kehn-Hall, K. Viral concentration determination through plaque assays: Using traditional and novel overlay systems. *J. Vis. Exp.* **2014**, *93*, 1–10. https://doi.org/10.3791/52065.
39. Audronis, M.; Jimenez, O.; Leyland, A.; Matthews, A. The morphology and structure of PVD ZrN-Cu thin films. *J. Phys. D. Appl. Phys.* **2009**, *42*, 085308. https://doi.org/10.1088/0022-3727/42/8/085308.
40. Jimenez, O.; Audronis, M.; Baker, M.A.; Matthews, A.; Leyland, A. Structure and mechanical properties of nitrogen-containing Zr-Cu based thin films deposited by pulsed magnetron sputtering. *J. Phys. D. Appl. Phys.* **2008**, *41*, 155301. https://doi.org/10.1088/0022-3727/41/15/155301.
41. Li, J.; Zhang, H.; Fan, A.; Tang, B. Tribological properties characterization of Ti/Cu/N Thin films prepared by DC magnetron sputtering on titanium alloy. *Surf. Coat. Technol.* **2016**, *294*, 30–35. https://doi.org/10.1016/j.surfcoat.2016.03.043.
42. Zeman, P.; Čerstvý, R.; Mayrhofer, P.H.; Mitterer, C.; Musil, J. Structure and properties of hard and superhard Zr-Cu-N nanocomposite coatings. *Mater. Sci. Eng. A* **2000**, *289*, 189–197. https://doi.org/10.1016/S0921-5093(00)00917-5.
43. Slater, J.C. Atomic radii in crystals. *J. Chem. Phys.* **1964**, *41*, 3199–3204. https://doi.org/10.1063/1.1725697.
44. Chen, T.; Yu, L.; Ju, H.; Xu, J.; Koyama, S. Influence of Cu Content on the Microstructure, Mechanical, and Tribological Properties of ZrN-Cu Films. *Nano* **2018**, *13*, 1850035. https://doi.org/10.1142/S1793292018500352.
45. Pierson, J.F.; Wiederkehr, D.; Billard, A. Reactive magnetron sputtering of copper, silver, and gold. *Thin Solid Film.* **2005**, *478*, 196–205. https://doi.org/10.1016/j.tsf.2004.10.043.
46. Nowakowska-Langier, K.; Chodun, R.; Minikayev, R.; Okrasa, S.; Strzelecki, G.W.; Wicher, B.; Zdunek, K. Copper nitride layers synthesized by pulsed magnetron sputtering. *Thin Solid Film.* **2018**, *645*, 32–37. https://doi.org/10.1016/j.tsf.2017.10.042.
47. Liu, Z.Q.; Wang, W.J.; Wang, T.M.; Chao, S.; Zheng, S.K. Thermal stability of copper nitride films prepared by rf magnetron sputtering. *Thin Solid Film.* **1998**, *325*, 55–59. https://doi.org/10.1016/S0040-6090(98)00448-9.
48. Rahmati, A.; Bidadi, H.; Ahmadi, K.; Hadian, F. Ti substituted nano-crystalline Cu3N thin films. *J. Coat. Technol. Res.* **2011**, *8*, 289–297. https://doi.org/10.1007/s11998-010-9279-9.
49. Maruyama, T.; Morishita, T. Copper nitride and tin nitride thin films for write-once optical recording media. *Appl. Phys. Lett.* **1996**, *69*, 890–891. https://doi.org/10.1063/1.117978.
50. Maya, L. Deposition of crystalline binary nitride films of tin, copper, and nickel by reactive sputtering. *J. Vac. Sci. Technol. A.* **1993**, *11*, 604–608. https://doi.org/10.1116/1.578778.
51. Wang, D.; Nakamine, N.; Hayashi, Y. Properties of various sputter-deposited Cu–N thin films. *J. Vac. Sci. Technol. A.* **1998**, *16*, 2084–2092. https://doi.org/10.1116/1.581314.
52. Pierson, J.F. Structure and properties of copper nitride films formed by reactive magnetron sputtering. *Vacuum* **2002**, *66*, 59–64. https://doi.org/10.1016/S0042-207X(01)00425-0.
53. Yue, G.H.; Yan, P.X.; Wang, J. Study on the preparation and properties of copper nitride thin films. *J. Cryst. Growth* **2005**, *274*, 464–468. https://doi.org/10.1016/j.jcrysgro.2004.10.032.
54. Musil, J.; Zeman, P.; Hrubý, H.; Mayrhofer, P.H. ZrN/Cu nanocomposite film—A novel superhard material. *Surf. Coat. Technol.* **1999**, *120*, 179–183. https://doi.org/10.1016/S0257-8972(99)00482-X.
55. Schiøtz, J.; Vegge, T.; Di Tolla, F.D.; Jacobsen, K.W. Atomic-scale simulations of the mechanical deformation of nanocrystalline metals. *Phys. Rev. B Condens. Matter Mater. Phys.* **1999**, *60*, 11971–11983. https://doi.org/10.1103/PhysRevB.60.11971.
56. Zhang, S.; Sun, D.; Fu, Y.; Du, H. Recent advances of superhard nanocomposite coatings: A review. *Surf. Coat. Technol.* **2003**, *167*, 113–119. https://doi.org/10.1016/S0257-8972(02)00903-9.
57. Santo, C.E.; Taudte, N.; Nies, D.H.; Grass, G. Contribution of copper ion resistance to survival of Escherichia coli on metallic copper surfaces. *Appl. Environ. Microbiol.* **2008**, *74*, 977–986. https://doi.org/10.1128/AEM.01938-07.
58. Kertzman, Z.; Marchal, J.; Suarez, M.; Staia, M.H.; Filip, P.; Kohli, P.; Aouadi, S.M. Mechanical, tribological, and biocompatibility properties of ZrN-Ag nanocomposite films. *J. Biomed. Mater. Res. Part A* **2008**, *84*, 1061–1067. https://doi.org/10.1002/jbm.a.31533.
59. Wißmann, J.E.; Kirchhoff, L.; Brüggemann, Y.; Todt, D.; Steinmann, J.; Steinmann, E. Persistence of pathogens on inanimate surfaces: A narrative review. *Microorganisms* **2021**, *9*, 343. https://doi.org/10.3390/microorganisms9020343.
60. Lanini, S.; D'Arezzo, S.; Puro, V.; Martini, L.; Imperi, F.; Piselli, P.; Montanaro, M.; Paoletti, S.; Visca, P.; Ippolito, G. Molecular epidemiology of a Pseudomonas aeruginosa hospital outbreak driven by a contaminated disinfectant-soap dispenser. *PLoS ONE* **2011**, *6*, e17064. https://doi.org/10.1371/journal.pone.0017064.
61. Dan, Z.G.; Ni, H.W.; Xu, B.F.; Xiong, J.; Xiong, P.Y. Microstructure and antibacterial properties of AISI 420 stainless steel implanted by copper ions. *Thin Solid Film.* **2005**, *492*, 93–100. https://doi.org/10.1016/j.tsf.2005.06.100.
62. Chin, A.W.H.; Chu, J.T.S.; Perera, M.R.A.; Hui, K.P.Y.; Yen, H.L.; Chan, M.C.W.; Peiris, M.; Poon, L.L.M. Stability of SARS-CoV-2 in different environmental conditions. *Lancet Microbe* **2020**, *1*, e10. https://doi.org/10.1016/S2666-5247(20)30003-3.
63. Warnes, S.L.; Little, Z.R.; Keevil, C.W. Human coronavirus 229E remains infectious on common touch surface materials. *MBio* **2015**, *6*, e01697-15. https://doi.org/10.1128/mBio.01697-15.
64. Warnes, S.L.; Keevil, C.W. Inactivation of Norovirus on Dry Copper Alloy Surfaces. *PLoS ONE* **2013**, *8*, e75017. https://doi.org/10.1371/journal.pone.0075017.
65. Warnes, S.L.; Summersgill, E.N.; Keevil, C.W. Inactivation of murine norovirus on a range of copper alloy surfaces is accompanied by loss of capsid integrity. *Appl. Environ. Microbiol.* **2015**, *81*, 1085–1091. https://doi.org/10.1128/AEM.03280-14.

66. Sagripanti, J.L.; Routson, L.B.; Lytle, C.D. Virus inactivation by copper or iron ions alone and in the presence of peroxide. *Appl. Environ. Microbiol.* **1993**, *59*, 4374–4376. https://doi.org/10.1128/aem.59.12.4374-4376.1993.
67. Govind, V.; Bharadwaj, S.; Sai Ganesh, M.R.; Vishnu, J.; Shankar, K.V.; Shankar, B.; Rajesh, R. Antiviral properties of copper and its alloys to inactivate covid-19 virus: A review. *BioMetals* **2021**, *34*, 1217–1235. https://doi.org/10.1007/s10534-021-00339-4.
68. Purniawan, A.; Lusida, M.I.; Pujiyanto, R.W.; Nastri, A.M.; Permanasari, A.A.; Harsono, A.A.H.; Oktavia, N.H.; Wicaksono, S.T.; Dewantari, J.R.; Prasetya, R.R.; et al. Synthesis and assessment of copper-based nanoparticles as a surface coating agent for antiviral properties against SARS-CoV-2. *Sci. Rep.* **2022**, *12*, 4835. https://doi.org/10.1038/s41598-022-08766-0.
69. van Doremalen, N.; Bushmaker, T.; Morris, D.H.; Holbrook, M.G.; Gamble, A.; Williamson, B.N.; Tamin, A.; Harcourt, J.L.; Thornburg, N.J.; Gerber, S.I.; et al. Aerosol and Surface Stability of SARS-CoV-2 as Compared with SARS-CoV-1. *N. Engl. J. Med.* **2020**, *382*, 1564–1567. https://doi.org/10.1056/NEJMc2004973.
70. Lishchynskyi, O.; Shymborska, Y.; Stetsyshyn, Y.; Raczkowska, J.; Skirtach, A.G.; Peretiatko, T.; Budkowski, A. Passive antifouling and active self-disinfecting antiviral surfaces. *Chem. Eng. J.* **2022**, *446*, 137048. https://doi.org/10.1016/j.cej.2022.137048.
71. Bregnocchi, A.; Jafari, R.; Momen, G. Design strategies for antiviral coatings and surfaces: A review. *Appl. Surf. Sci. Adv.* **2022**, *8*, 100224. https://doi.org/10.1016/j.apsadv.2022.100224.